

Nanocrystalline intermetallics on mesoporous carbon for direct formic acid fuel cell anodes

Xiulei Ji¹, Kyu Tae Lee¹, Reanne Holden¹, Lei Zhang², JiuJun Zhang², Gianluigi A. Botton³, Martin Couillard³ and Linda F. Nazar^{1*}

Shape- and size-controlled supported metal and intermetallic nanocrystallites are of increasing interest because of their catalytic and electrocatalytic properties. In particular, intermetallics PtX (X = Bi, Pb, Pd, Ru) are very attractive because of their high activity as fuel-cell anode catalysts for formic acid or methanol oxidation. These are normally synthesized using high-temperature techniques, but rigorous size control is very challenging. Even low-temperature techniques typically produce nanoparticles with dimensions much greater than the optimum <5 nm required for fuel cell catalysis. Here, we present a simple and robust, chemically controlled process for synthesizing size-controlled noble metal or bimetallic nanocrystallites embedded within the porous structure of ordered mesoporous carbon (OMC). By using surface-modified ordered mesoporous carbon to trap the metal precursors, nanocrystallites are formed with monodisperse sizes as low as 1.5 nm, which can be tuned up ~3.5 nm. To the best of our knowledge, 3-nm ordered mesoporous carbon-supported PtBi nanoparticles exhibit the highest mass activity for formic acid oxidation reported to date, and over double that of Pt-Au.

Q1

Much attention has recently been focused on low-temperature fuel cells with energy conversion based on formic acid (HCOOH) instead of methanol^{1,2}, because HCOOH exhibits much lower crossover flux through Nafion[®] membranes³. However, such cells require a bimetallic catalyst at the anode (fuel) side, because conventional catalysts such as platinum are readily poisoned by the CO that is produced as a side product^{4,5}. This serious self-poisoning^{6,7} is explained by the 'dual-path reaction mechanism'⁸. In the desirable path, sequential dehydrogenation steps lead to the direct formation of CO₂ from formic acid (path 1). In the undesirable path, CO, formed as a reaction intermediate via dehydration (path 2), readily adsorbs onto the platinum surface, and impedes further fuel oxidation. It is widely believed that the dehydration path requires the presence of platinum atom ensembles—continuous neighbouring atomic sites—whereas the dehydrogenation path does not⁹. This explains the poor properties of platinum metal. Furthermore, the CO poisoning effect can be inhibited by the breach of platinum ensembles. By using bulk platinum with adatoms on the surface^{10–14} or bulk PtM (M: Bi, Pb, Pd) intermetallic catalysts^{15–17}, resistance to CO poisoning of the catalysed formic acid oxidation was improved. Catalyst composition is not the only important factor. To prepare an efficient gas diffusion electrode, the catalyst particles must have nanoscale dimensions, are ideally monodisperse, and should be supported on porous carbon. Nanoparticles are necessary to achieve high mass activity and complete resistance to CO poisoning. Literature reports cite difficulty in synthesizing intermetallics in nanocrystalline form at low temperatures where sintering does not result in particle aggregation, although some progress has been achieved. By applying the polyol process¹⁸ or a co-reduction method using sodium borohydride^{19,20}, DiSalvo, Abruña and colleagues generated unsupported intermetallic PtBi and PtPb nanoparticles (~20 nm or larger). Although the mass activity of these catalysts was not maximized due to particle agglomeration, nearly complete elimination of CO poisoning was observed. Special synthetic procedures are required to avoid

Q2

agglomeration of the alloy nanoparticles that are normally formed at high temperatures. Recently, new advances in particle size control of supported intermetallic materials have been reported. Schaak and colleagues introduced the preparation of supported intermetallic nanocrystals, including PtBi, by using pre-formed supported single metal nanoparticles as nucleation sites²¹. However, upon annealing to nucleate intermetallic phases, these unconfined metal particles typically grow larger than desired. To date, major efforts have been devoted to particle size control of intermetallic nanoparticles, with only limited success. Another difficulty is in preparing the catalysts directly supported on carbon, while simultaneously achieving good crystallite size control. It is well known that the performance of a catalyst layer in a fuel cell is influenced by where and how these particles are supported²². A good catalyst support should be efficient in charge and mass transfer, and capable of inhibiting sintering and loss of the catalyst during operation. Improvements in the development of supported catalysts based on intermetallics requires a reliable methodology that facilitates not only particle size control but the fine dispersion of these nanoparticles on a support such as ordered mesoporous carbon (OMC)²³.

OMCs have many desirable characteristics, including interconnected porous structures, narrow pore size distributions and high surface areas, and have attracted much attention for their application as catalyst supports for fuel cells^{24–27}. To maximize the mass activity of a catalyst and take advantage of the unique architectures of the OMC, it is vital that the catalyst nanoparticles be loaded within the mesoporous voids. This has proven very challenging. The so-called 'wet' process—the only route explored to date^{24,28}—is limited by the poor compatibility between the hydrophobic carbon and the hydrophilic solvents necessary to dissolve the catalyst precursors. This results in heterogeneous particle size distribution both within and on the outer surface of the OMC. To solve this problem, one approach is to transform the OMC into a more hydrophilic material^{29,30}. However, successful modification

¹University of Waterloo, Department of Chemistry, Waterloo, Ontario, Canada N2L 3G1, ²Institute for Fuel Cell Innovation, National Research Council Canada, Vancouver, British Columbia, Canada V6T 1W5, ³McMaster University, Department of Materials Science and Engineering, Hamilton, Ontario, Canada L8S 4L8. *e-mail: lfnazar@uwaterloo.ca

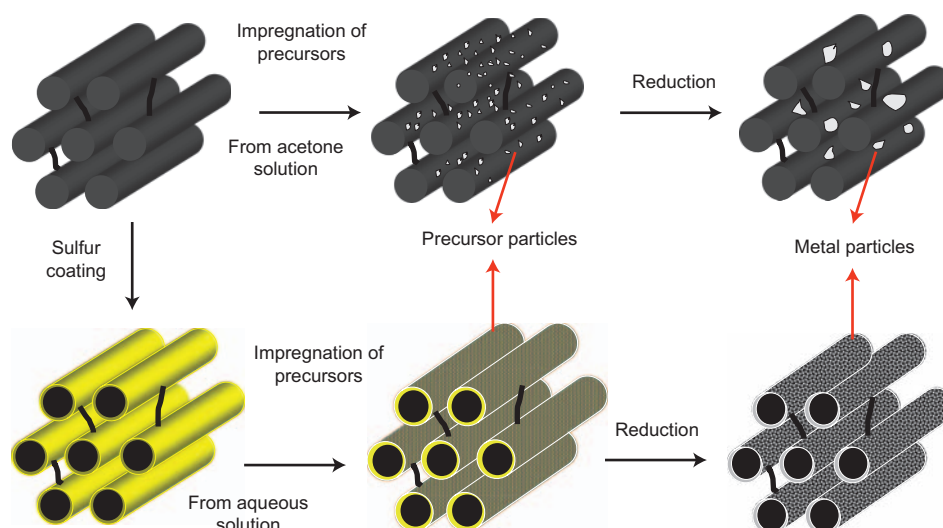


Figure 1 | Schematic illustrating the nucleated-growth synthesis of OMC-supported noble metal and intermetallic nanocrystallites. **a**, The conventional impregnation method used to load noble metal nanoparticles into OMC. **b**, The present impregnation method, using sulfur-functionalized OMC to act as a metal trap to nucleate noble metals (Pt, Pd, Ru, Rh) or intermetallics (PtBi).

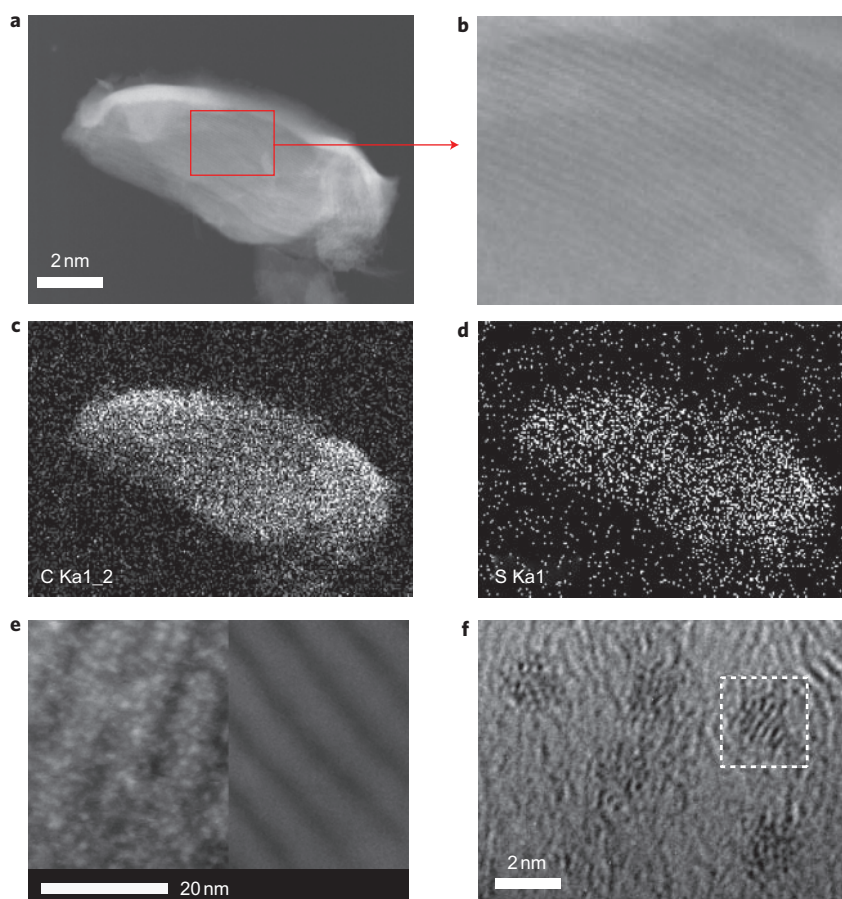


Figure 2 | TEM images demonstrating the formation of OMC-supported platinum nanocrystallites with dimensions of $< 2\text{ nm}$. **a**, STEM overview of OMC-S. **b**, Image expansion corresponding to the area outlined by the red square in **a**. **c,d**, Corresponding carbon and sulfur elemental maps using EDX. **e**, Composite image comparing OMC-Pt-1.5 nm (left) and pristine OMC (right). **f**, Bright-field HRTEM image of OMC-Pt-1.5 nm.

1 of OMCs that facilitates metal nanoparticle loading has not been
 2 reported³¹. As an alternative approach, one-pot synthesis of plati-
 3 num-based nanoparticles has recently been investigated^{32–36}.
 4 Typically, these nanoparticles are wrapped within the walls of

mesoporous structures. They show improved methanol tolerance 5
 as cathode catalysts for direct methanol fuel cells, but suffer from 6
 poor accessibility of the catalysts. Here, we introduce a highly 7
 reliable synthetic strategy that enables a wide range of noble metal 8

1 or intermetallic nanoparticles to be encapsulated within the OMC
 2 voids, resulting in ultrafine dispersion and narrow particle size dis-
 3 tribution, giving excellent access to the catalyst centres. The encap-
 4 sulated intermetallic PtBi exhibits excellent performance in formic
 5 acid oxidation.

6 Results and discussion

7 Our proof-of-concept studies are based on CMK-3, a well investi-
 8 gated OMC³⁷, as illustrated in Fig. 1. In a departure from any pre-
 9 viously reported approaches, we modified the carbon surface with
 10 sulfur (OMC-S), which functions as a metal trap. Normally con-
 11 sidered to be a potent catalyst poison, sulfur exhibits a strong affinity
 12 for noble metals owing to a soft acid–soft base interaction^{38,39}. A
 13 thin layer of sulfur on OMC is used as a mediator that acts to
 14 absorb and bind the catalyst metal precursors from solution into
 15 the OMC, and additionally restricts their particle growth during
 16 reduction to result in ultrafine dispersions of metal nanocrystallites.
 17 The sulfur is readily imbibed by capillary forces into the OMC
 18 nanofibres from a sulfur melt, as we have demonstrated previously⁴⁰.
 19 Although sulfur/composite fractions up to 79 wt% sulfur can be
 20 prepared, which corresponds to complete filling of the empty chan-
 21 nels⁴⁰, here, the sulfur/carbon ratio is optimized at a much lower
 22 level (10 wt% sulfur/composite) to provide a thin coating on the
 23 interior surfaces. An annular dark-field scanning transmission elec-
 24 tron microscopy (STEM) image (Fig. 2a), together with energy-dis-
 25 persive X-ray (EDX) carbon and sulfur maps of the same particle
 26 (Fig. 2c,d), reveal a homogeneous distribution of sulfur in the
 27 OMC-S. We conclude that sulfur is homogeneously distributed
 28 within the interior, as no sulfur ‘halo’ is formed on the edges of
 29 the composite particle that would be indicative of an exterior
 30 coating. An image expansion (Fig. 2a,b) on a sulfur-populated
 31 area (Fig. 2d) shows ordered channels with no contrast variation.
 32 This suggests that sulfur molecules form a thin layer on the
 33 surface of the carbon nanorods without forming aggregates that
 34 block the channels. This is in agreement with our previous
 35 studies, which indicate that sulfur wets carbon very readily⁴⁰. The
 36 successful loading and ultrafine dispersion of metal and intermetal-
 37 lic nanoparticles into the channels of the mesoporous carbon
 38 further supports the existence of the thin sulfur layer. Preservation
 39 of the long-range ordering of the channels is further confirmed by
 40 low angle X-ray diffraction (XRD; Supplementary Fig. S1a,ii).

41 We first sought to deposit platinum nanocrystallites to serve as
 42 proof of concept. Aqueous solutions of H_2PtCl_6 were contacted
 43 with the sulfur-mediated OMC-S. For comparison, solutions of
 44 H_2PtCl_6 in acetone were contacted with unmodified OMC to
 45 form ‘conventional’ platinum-loaded OMC²⁴. The platinum-
 46 sorbed materials were treated in a reducing atmosphere of 7%
 47 H_2/N_2 . Thermogravimetric analysis differential scanning calorim-
 48 etry (TGA-DSC) measurements in air showed that sulfur is still
 49 present in the OMC-Pt composite following reduction to the
 50 metal at 350 °C (Supplementary Fig. S2a,b). It functions as
 51 the necessary stabilizing agent to inhibit platinum nucleation in
 52 the initial stages. The residual sulfur, which would otherwise
 53 destroy catalytic activity, is then completely removed by evacuation
 54 at 300 °C for 12 h. Its absence was determined by TGA-DSC
 55 (OMC-Pt only exhibits carbon weight loss; Supplementary
 56 Fig. S2c) and confirmed by the absence of any S [2p] signals in
 57 X-ray photoelectron spectra (XPS) of OMC-Pt (Fig. 3a). Samples
 58 were etched by Ar^+ sputtering sec to obtain XPS signals from
 59 regions within the OMC-Pt composite. Further proof of complete
 60 sulfur removal was demonstrated by the high catalytic activity of
 61 the materials (see below). The metallic nature of the platinum is
 62 also demonstrated by the characteristic platinum [4f] signal in the
 63 XPS spectra (Fig. 3b).

64 A significantly higher degree of platinum dispersion within
 65 channels of OMC prepared by the sulfur-entrapment route was

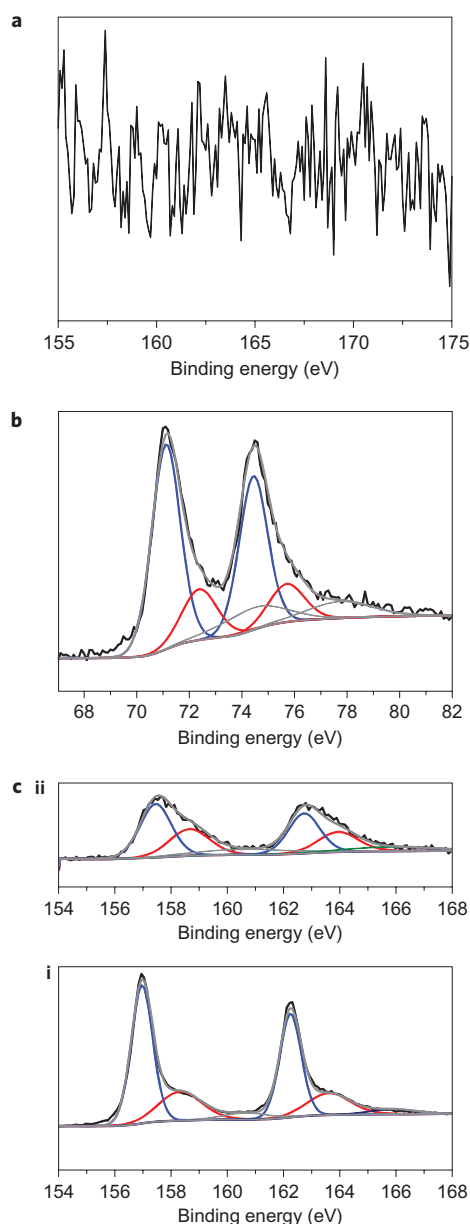


Figure 3 | XPS spectra of platinum and PtBi nanocrystallites supported on OMC. **a**, Sulfur [2p] signal from OMC-Pt-2 nm, demonstrating the lack of sulfur residue. **b**, Platinum [4f] signal from OMC-Pt-2 nm, with deconvolution into metallic platinum (blue trace) and Pt-O_x (surface contamination; red trace) components. **c**, Comparison of bismuth [4f] signals from bulk PtBi (i) and OMC-PtBi-3 nm (ii), showing the same high energy shift compared to metallic bismuth. The signals are deconvoluted into bismuth (blue trace) and Bi-O_x (surface contamination; red trace) components.

66 achieved compared to the conventional wet-casting method using
 67 acetone as a solvent for impregnation²⁴. Supplementary Fig. S1b
 68 shows the XRD pattern of conventionally prepared CMK-3/platinum
 69 composites. The reflections can be manually deconvoluted
 70 into two components. The first, highly broadened, is attributed to
 71 platinum domains 1–2 nm in size. The second sharper component
 72 arises from platinum domains with a coherence length of 6 nm, as
 73 calculated by Scherrer line broadening. This larger domain size
 74 is double that of the CMK-3 channel size, indicating that the particles
 75 are located on the external surface of the CMK-3 or their particle
 76 growth causes structural damage in the CMK-3. The poor

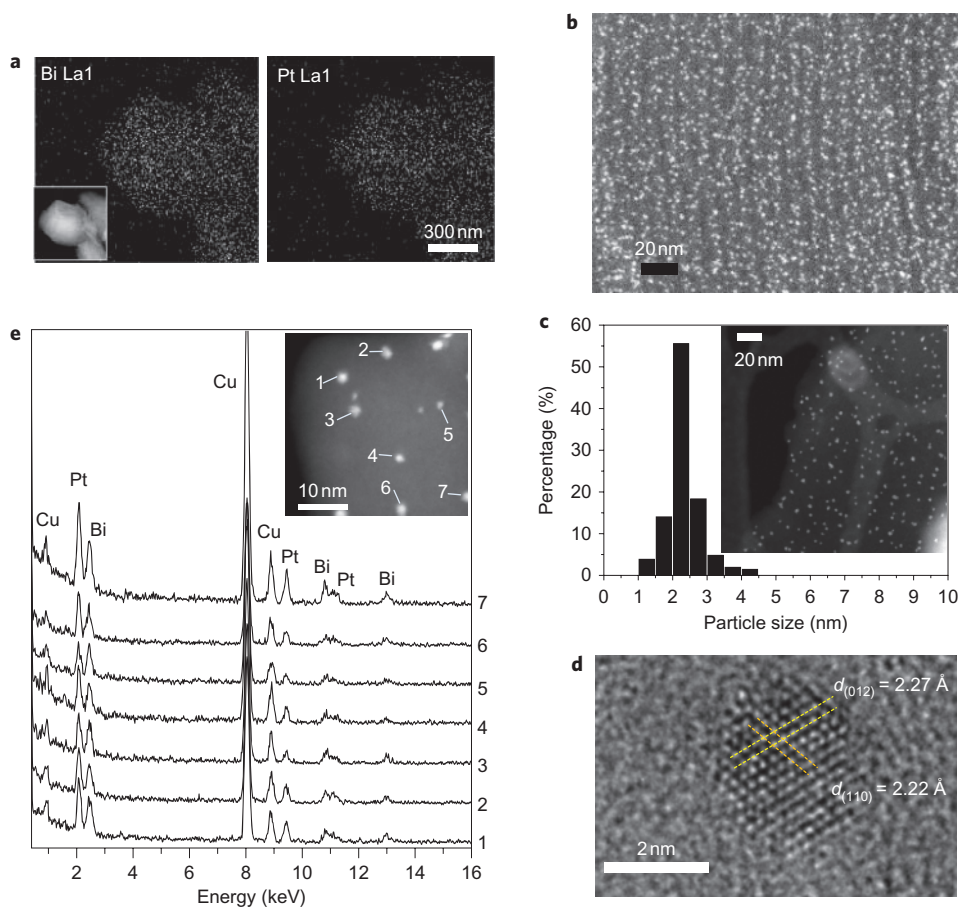


Figure 4 | TEM images and EDX maps of OMC-PtBi, revealing homogeneously dispersed 2–3 nm crystallites of the ordered intermetallic phase.

a, Platinum and bismuth EDX maps corresponding to their dark-field STEM image (inset), showing sub-nanometre mixing in the mesoporous carbon. **b**, Dark-field STEM image of OMC-PtBi-3 nm, illustrating the narrow crystallite size distribution in a representative section of the bulk. **c**, Histogram showing nanocrystallite size distribution based on a count of 407 crystallites in two different sample areas (representative STEM image shown in the inset). **d**, Bright-field HRTEM image of OMC-PtBi-3 nm, with lattice spacings marked. **e**, EDX spectra for individual PtBi nanoparticles in OMC-PtBi-3 nm; the inset shows the dark-field STEM image, with the corresponding analysed nanoparticles labelled.

1 compatibility between metal precursor solutions and carbon
 2 induces the inhomogeneity in the particle formation. In contrast,
 3 the OMC-Pt (24 wt% platinum/composite) derived from OMC-S
 4 exhibits a very narrow particle size distribution and ultrafine dispersion
 5 compared to the empty channels of OMC-S, as shown
 6 in Fig. 2e. A representative high-resolution transmission electron
 7 microscopy (HRTEM) image of these nanocrystallites is shown in
 8 Fig. 2f, revealing an average diameter of 1–2 nm. These particles
 9 do not disrupt the internal carbon framework because they are
 10 smaller than the channel dimensions. The well-preserved long-
 11 range order of the carbon walls in OMC-Pt is evident in the
 12 annular dark-field STEM image (Fig. 2e) and confirmed by the
 13 sharp peaks in the low-angle XRD pattern compared to those of
 14 the OMC-S and CMK-3 (Supplementary Fig. S1a). Furthermore,
 15 the size of the platinum particles can be controlled by heat treatment
 16 up to the size of the OMC channels, that is, ~3.5 nm. For example,
 17 platinum particles prepared at 350 °C can be increased in size from
 18 less than 2 nm (OMC-Pt-1.5 nm) to ~2 nm within 2 h under argon
 19 at 600 °C (Supplementary Fig. S3a) and to ~3.5 nm within 30 min
 20 at 800 °C (Supplementary Fig. S3b), as shown by HRTEM. Well-
 21 defined lattice fringes (scarcely detectable over the background
 22 intensity of the OMC for the smallest crystallites) are clearly
 23 evident in these larger crystallites (Supplementary Fig. S3).

24 Although the synthesis of OMC-supported platinum nanocrystallites
 25 demonstrates the viability of the methodology, our ultimate
 26 goal lies in the preparation of intermetallic or bimetallic

nanocatalysts in OMC channels; at present, these cannot be realized
 by other methods. For many applications including formic acid oxidation
 for fuel cell anodes, platinum- or palladium-based intermetallic
 nanomaterials based on main group metals such as bismuth are
 of particular interest. Our route works unusually well, because
 it relies on the use of the OMC-S bonded platinum to act as a
 nucleation site for bismuth. This is akin to reports that use platinum
 crystals deposited on carbon to provide a growth centre for subsequent
 alloying with bismuth (ref. 21). The difference in our case is that the
 platinum clusters generated *in situ* within the carbon channels
 orchestrate the assembly of nearby bismuth atoms produced during
 reduction into an ordered intermetallic phase. In the absence of
 platinum, reduction of OMC-Bi(NO₃)₃ under H₂/N₂ at 350 °C
 produces bulk bismuth metal (not nanobismuth) that forms external
 to the OMC-S, as shown by the XRD pattern (Supplementary Fig. S4a).
 This is due to the low melting temperature of bismuth (271.5 °C).
 Newly formed bismuth clusters agglomerate into large droplets to
 decrease their surface tension, unless they can immediately form a
 solid phase with nearby incipient platinum clusters. A TEM image
 of the material heated at 350 °C for 3 h (Supplementary Fig. S5a),
 together with the EDX elemental maps (Fig. 4a) and bismuth are
 homogeneously distributed in the ordered mesoporous framework
 and are intimately mixed. The crystallite size was estimated
 roughly to be 1–2 nm from an expanded section of the image
 (OMC-PtBi-1.5 nm). To further crystallize the

Q4

1 intermetallic structure (24 wt% total metal/composite), the material
 2 was heated in argon at 600 °C for 2 h. This resulted in uniform
 3 growth of the PtBi to form slightly larger, well-dispersed crystallites
 4 (Fig. 4b). A transition from PtBi-1.5 nm to larger, more ordered
 5 nanocrystallites upon heat treatment is also evident from XRD
 6 (Supplementary Fig. S1c,ii,iii), giving rise to sharpened reflections.
 7 Although there is a considerable degree of peak broadening owing
 8 to the very small crystallite size, the reflections exhibited by
 9 OMC-PtBi-3 nm are in good agreement with that of bulk PtBi
 10 (ref. 41), and do not match that of either end member phase (plati-
 11 num or bismuth) or any of their oxides. Further proof was provided
 12 by HRTEM (Fig. 4d showing a representative image of ~2.7 nm
 13 PtBi). The particles are crystalline and almost spherical in shape,
 14 as can be seen from the lattice fringes in the HRTEM. The lattice
 15 spacing and angle (~60°) of the two visible set of fringes correspond
 16 to the (012) and (110) planes of PtBi: [(012), 2.21 Å expected,
 17 2.21 Å observed; (110), 2.15 Å expected, 2.16 Å observed; see also
 18 Supplementary Fig. S5]. These planes are unique for PtBi
 19 (Supplementary Fig. S5). A lower-magnification STEM image and
 20 a corresponding histogram of the particle number distribution are
 21 shown in Fig. 4c. On counting ~400 particles, the average diameter
 22 was found to be 2.25 ± 0.5 nm, as shown in the histogram. We term
 23 these OMC-PtBi-3 nm. EDX measurements were conducted on
 24 single particles from different areas of the sample using a FEI
 25 Titan STEM equipped with an aberration corrector for the electron
 26 probe and a high-brightness electron source. The EDX spectra and
 27 high-angle annular STEM image (Fig. 4e, inset) unequivocally
 28 demonstrate the existence of both platinum and bismuth (at a
 29 ratio of ~1:1) in each crystallite. An additional set of spectra from
 30 a second region (Supplementary Fig. S6a) provided the same
 31 results, as did simultaneous sampling of many particles over a
 32 larger area. No Pt–Bi signal is observed in regions devoid of PtBi
 33 nanocrystallites (Supplementary Fig. S6b).

34 XPS spectra were also collected for composite materials. The
 35 carbon 1s signal served as an internal reference. As shown in
 36 Fig. 3c, both bulk PtBi and OMC-PtBi-3 nm exhibit a Bi $4f_{7/2}$
 37 signal that can be deconvoluted into two components. The minor
 38 signal at 158.4 eV is attributed to surface Bi_xO_y, formed during trans-
 39 fer of the sample in air to the XPS chamber (an oxide component is
 40 also apparent in the Pt 4f spectrum, Fig. 3b). The major component at
 41 157.0–157.2 eV lies at a higher energy when compared to that of pure
 42 bismuth metal supported on OMC (156.7 eV), and is characteristic of
 43 PtBi, as reported elsewhere⁴². Note that nano-PtBi is also very slightly
 44 shifted to higher energy compared to bulk-PtBi.

45 Steady-state cyclic voltammograms (CV) of formic acid oxida-
 46 tion on the different catalysts, at a scan rate of 10 mV s⁻¹, are pre-
 47 sented in Fig. 5. For OMC-Pt-2 nm, the first current maximum at
 48 0.68 V (versus a reversible hydrogen electrode, RHE) in the
 49 anodic scan is assigned to the ‘direct path’ reaction (path 1, see
 50 above; Fig. 5a, black line). The second current maximum at
 51 0.94 V, with a hysteresis, corresponds to oxidation of CO_{ad}, accu-
 52 mulated in the ‘CO path’ (path 2, see above). The ratio between
 53 the intensities of the two peaks sheds light on the question of
 54 which path is adopted more during the catalysis process. With the
 55 poisoning species consumed in the anodic scan, the current
 56 attains a higher maximum in the subsequent cathodic scan. A CV
 57 of formic acid oxidation on conventionally prepared CMK-3/plati-
 58 num (that is, OMC/platinum without sulfur mediation), carried out
 59 under the same conditions, was also performed (Fig. 5a, red line).
 60 OMC-Pt-2 nm is clearly superior to CMK-3/platinum. It exhibits
 61 a lower onset potential, a higher current maximum for formic
 62 acid oxidation, and a higher versus peak ratio. This demonstrates
 63 that the sulfur used in catalyst preparation is fully removed and
 64 does not contaminate or poison the surface.

65 Figure 5b shows the voltammograms of formic acid oxidation on
 66 OMC-PtBi-1 nm and OMC-PtBi-3 nm. The catalytic performance

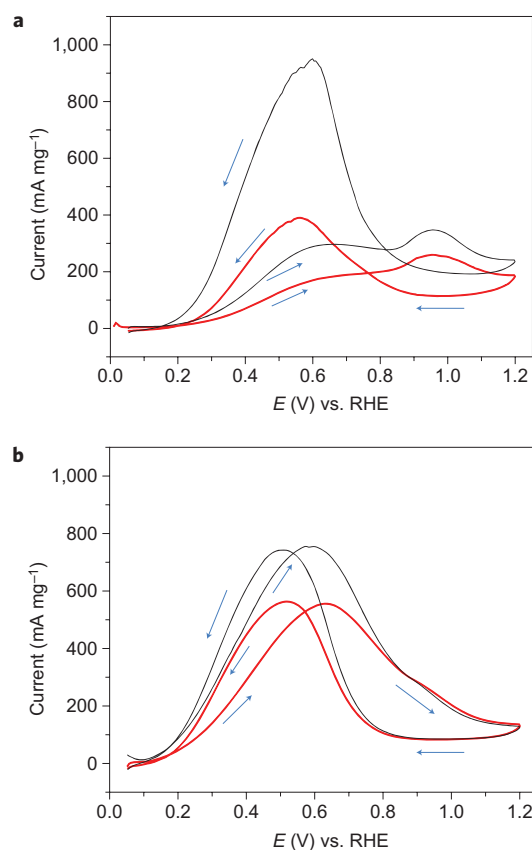


Figure 5 | Steady-state cyclic voltammograms obtained for formic acid oxidation. **a**, CMK-3/platinum (red line) and OMC-Pt-2 nm (black line). **b**, OMC-PtBi-1 nm (red line) and OMC-PtBi-3 nm (black line) in 0.5 M sulfuric acid/0.5 M formic acid solution (scan rate 10 mV s⁻¹). The electrochemical response, which is nearly identical in the forward and reverse sweeps, shows an exceptionally high mass activity.

67 closely resembles that of palladium/carbon catalysed formic acid
 68 oxidation, where palladium is reported to be favourable to dehydro-
 69 genation of formic acid without the formation of CO^{43,44}. The
 70 current behaviour of formic acid oxidation in scans in both direc-
 71 tions is nearly identical, which is a significant improvement over
 72 the pure platinum case¹⁵, or ‘large-nano’ intermetallic PtBi on
 73 carbon¹⁶. The results indicate that the dehydrogenation path is com-
 74 pletely eliminated for these OMC-PtBi catalysts. OMC-PtBi
 75 materials exhibit an onset potential of ~0.08 V, which is 0.12 V
 76 lower than that of OMC-Pt-2 nm, indicating that formic acid oxida-
 77 tion is catalysed more easily on PtBi nanoparticles than on pure
 78 platinum. OMC-PtBi-3 nm displays superior properties to those
 79 of OMC-PtBi-1 nm by exhibiting both a higher current maximum
 80 at a lower potential (0.57 V versus RHE). The improved crystallinity
 81 of the 2–3 nm PtBi particles compared with the 1 nm PtBi explains
 82 their superior properties. Furthermore, OMC-PtBi-3 nm exhibits a
 83 very high mass activity of 770 mA mg⁻¹ at 0.57 V, which is double
 84 that of recently reported platinum-decorated gold nanoparticles
 85 (400 mA mg⁻¹)⁴⁵ and PtAg alloy nanoparticles (340 mA mg⁻¹)⁴⁶
 86 under the same conditions used here.

87 Chronoamperometry (CA) was carried out at a practical operat-
 88 ing voltage of 0.3 V versus RHE to investigate the long-term stability
 89 of OMC-PtBi-3 nm. The CA curve (Supplementary Fig. S7) shows a
 90 high activity (800 mA mg⁻¹) with a deactivation rate of ~5%/100 s
 91 in the first 1,000 s. This is comparable to that of 3 nm palladium
 92 nanoparticles/OMC, which exhibits a deactivation rate of
 93 4.5%/100 s in the same time period⁴⁴. At the end of the first
 94 hour, a mass activity of 220 mA mg⁻¹ is achieved, and the

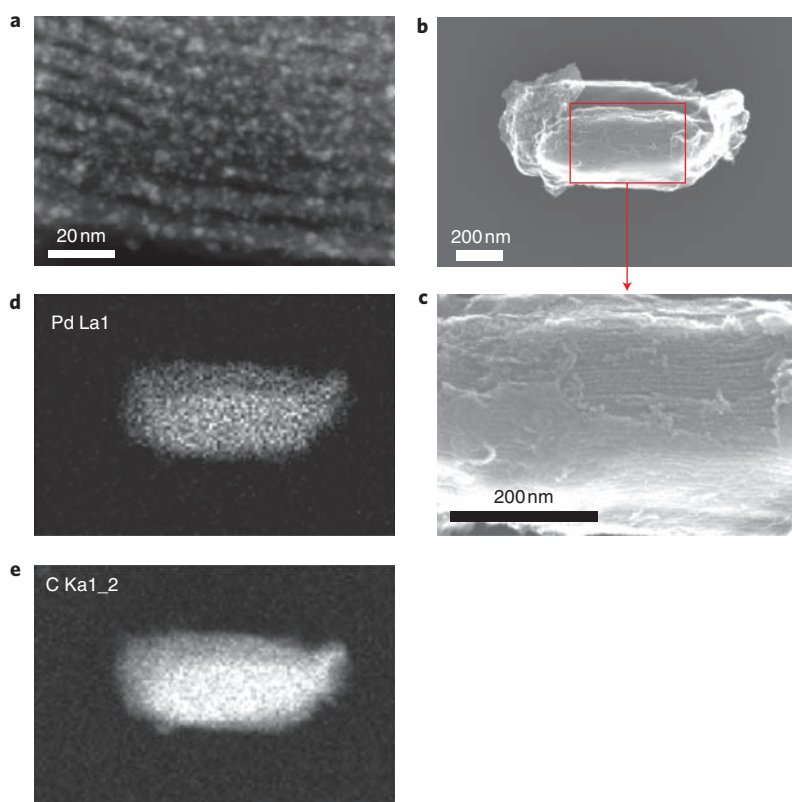


Figure 6 | TEM and SEM images and an elemental map of nanocrystalline palladium (<3 nm) supported on OMC, prepared by the sulfur-functionalized OMC strategy. **a**, TEM image (annular dark-field STEM). **b**, SEM image. **c**, Image expansion corresponding to the area outlined by the red square in **b**. **d**, Palladium map corresponding to **b**. **e**, Carbon map corresponding to **b**.

1 current decay diminishes over the next 2 h to fully stabilize at
 2 100 mA mg⁻¹. Stability tests on other bulk PtBi and PtBi nanopar-
 3 ticles have not been reported, to our knowledge. Compared to pure
 4 platinum, which typically loses 80% of its activity in the first 60 s
 5 (ref. 47), the PtBi nano-intermetallic shows much higher mass
 6 activity and better resistivity to poisoning over the long term, as
 7 expected. When compared with state-of-the-art catalysts (for
 8 which stability data have been reported), OMC-PtBi-3 nm also exhi-
 9 bits good performance. It has a higher activity per gram with a
 10 similar deactivation rate when compared to Pt₈₀Ru₂₀ nanopar-
 11 ticles⁴⁸ and PtPd nanoparticles¹⁷, and is comparable to that of
 12 other carbon-supported 6 nm palladium nanoparticles⁴⁹. To the
 13 best of our knowledge, other than the nano-catalysts mentioned
 14 above, most either exhibit very low activity with higher stability⁴³
 15 or suffer very fast current deactivation⁵⁰. To date, simultaneously
 16 achieving high stability and very high activity remains a challenge.
 17 It not only requires highly developed synthetic techniques, but
 18 also a more comprehensive understanding of the formic acid oxi-
 19 dation catalytic process.

20 Our preparation methodology is also widely applicable to many
 21 noble metals. With OMC-S as a support, several examples of OMC-
 22 M (12 wt% M/composite; M = Pd, Rh, Ru) were all successfully
 23 fabricated. These nanocrystalline composites also exhibit a narrow
 24 particle size distribution and a very fine dispersion on the order
 25 of ~2 nm, as shown in their TEM images (Fig. 6a; Supplementary
 26 Figs S8d, S9d). In SEM images, these composites exhibit very
 27 clean and ordered surface morphology, indicating that the nanopar-
 28 ticles are well confined (Fig. 6b,c; Supplementary Figs S8a,b, S9a,b).
 29 The corresponding elemental maps of these composites identify that
 30 these metal particles are homogeneously distributed in the frame-
 31 work of the OMC (Fig. 6b,d,e; Supplementary Figs S8a,c, S9a,c).
 32 These materials are of interest as potential supercapacitor electrodes

(ruthenium), methanol oxidation/formic acid fuel cell catalysts 33
 (palladium) or as heterogeneous catalysts for organic syntheses. 34

In conclusion, we describe a novel, highly effective methodology 35
 for impregnating noble metal and bimetallic nanoparticles into 36
 OMC voids with precisely controlled particle size and ultrahigh dis- 37
 persion. The method is applicable to a wide range of catalysts, 38
 namely bimetallic PtBi, but also platinum, ruthenium, rhodium 39
 and palladium. It is evident that intermetallics less than 3.5 nm in 40
 diameter can be formed in the channels of OMC with this approach. 41
 OMC-PtBi nano-hybrids were investigated as catalysts for formic 42
 acid oxidation for the first time. OMC-PtBi catalysts show an 43
 absence of CO poisoning. It is one of the most stable catalysts reported 44
 for formic acid oxidation, with similarly highest level of mass 45
 activity under the same conditions. The excellent catalytic proper- 46
 ties can be attributed to successful catalyst preparation and the faith- 47
 ful occurrence of the ‘ensemble effect’ at the nanoscale level. 48
 Although the concept is illustrated here with nanocrystalline PtBi, 49
 the generality of this process dictates that a variety of intermetallics 50
 having at least one component that strongly interacts with sulfur 51
 could also be developed for bi- and trimetallic nanocrystallites. 52
 These can be supported on a variety of conventional and new 53
 porous carbons, using this approach, with a view to use in a 54
 broad set of applications including electrocatalysis and catalysis. 55
 Ongoing work in our laboratory on other nanocrystalline PtX and 56
 trimetallic systems will be reported in forthcoming publications. 57

Methods 58

Synthesis of OMC-S and OMC catalysts. CMK-3 was prepared using a nanocasting 59
 method³⁷ following the well-established procedure in the literature and with SBA-15 60
 (ref. 43) as a hard template. Nanocomposite OMC-S was prepared following a melt- 61
 diffusion strategy⁴⁰. Typically, 0.1 g of sulfur and 0.9 g of CMK-3 were ground 62
 together, and the impregnation was carried out at 155 °C. OMC-S was impregnated 63
 with catalyst precursors by dispersed it in aqueous solutions containing the desired 64

1 concentration of metal precursors ($\text{H}_2\text{PtCl}_6 \cdot 6\text{H}_2\text{O}$, and $\text{Pd}(\text{NO}_3)_2 \cdot 2\text{H}_2\text{O}$).
2 Ethylene glycol was used to solvate precursors that easily hydrolyse in water, such as
3 $\text{Bi}(\text{NO}_3)_3 \cdot 5\text{H}_2\text{O}$, $\text{RuCl}_3 \cdot \text{H}_2\text{O}$ and $\text{RhCl}_3 \cdot \text{H}_2\text{O}$. The mixture of OMC-S and
4 precursor solution was stirred for 6 h before the solvents were evaporated. The
5 reduction of metal precursors was completed under a flow of 7% H_2/N_2 at 350 °C for
6 3 h. Samples were evacuated at 300 °C for 12 h to completely remove adsorbed H_2
7 and sulfur. Higher temperatures were also used for subsequent heat treatment, as
8 indicated in the text.

9 To compare the platinum loaded on OMC-S prepared by our sulfur mediation
10 route with conventionally prepared material, 24 wt% platinum-loaded OMC
11 was prepared using a solution of H_2PtCl_6 in acetone, strictly following the
12 literature procedure²⁴.

13 For the preparation of bulk PtBi, $\text{H}_2\text{PtCl}_6 \cdot 6\text{H}_2\text{O}$ and $\text{Bi}(\text{NO}_3)_3 \cdot 5\text{H}_2\text{O}$ with a
14 molar ratio of 1:1 were completely dissolved in ethylene glycol to achieve mixing at
15 the molecular level. The solvent was then evacuated and the precursor mixture
16 heated at 600 °C for 12 h under a flow of 7% H_2/N_2 .

17 **Characterization.** X-ray diffraction patterns at low (0.75 to 4° in 2 θ) and wide angle
18 (from 20 to 70° in 2 θ) were collected on a D8-ADVANCE powder X-ray
19 diffractometer operating at 40 kV and 30 mA and using Cu-K α radiation ($\lambda =$
20 0.15406 nm). The dark-field STEM was carried out with a Hitachi HD-2000 STEM.
21 All the bright-field high-resolution TEM images and EDX spectra for individual
22 2–3 nm nanocrystallines based on corresponding bright-field STEM images were
23 carried out on a FEI TitanTM 80–300 equipped with an aberration corrector for the
24 imaging lens and monochromator and also a FEI TitanTM 80–300 Cubed equipped
25 with a high-brightness electron source, aberration correctors of the probe-forming
26 lens and of the imaging lens, as well as a monochromator. High-resolution imaging
27 on the Titan 80–300 was carried out at 300 keV after tuning the aberration corrector
28 to achieve 0.08-nm resolution in standard Young's fringes experiments. EDX
29 measurements on the Titan 80–300 Cubed were obtained at 80 keV to minimize
30 electron-beam irradiation occurring due to the use of the high-brightness electron
31 source. Spectra of individual particles were collected for 300 s each while the electron
32 beam was kept rastering on the selected individual particle so as to remove any effect
33 of sample drift during the long acquisition time. Alignment of the system for annular
34 dark-field imaging was carried out with the standard probe-corrector alignment
35 procedure using gold cross-grating to achieve an imaging resolution better than
36 0.1 nm (ultimate information transfer better than 0.07 nm). XPS was carried out
37 using a Thermo Scientific K-Alpha XPS spectrometer with a monochromatic
38 Al K α source (1,486.6 eV), capable of an energy resolution of 0.4–0.5 eV full-width
39 at half-maximum.

40 **Electrochemical measurements.** For the preparation of working electrodes, 10.0 mg
41 of metal/mesoporous carbon composite (24 wt% metal) was suspended in 5.0 ml of
42 2-propanol, and then ultrasonically blended for 30 min to form the catalyst ink.
43 Exactly 10 μl of this catalyst ink was pipetted onto the surface of the glassy carbon
44 disk electrode (geometric area of 0.196 cm²). The catalyst-coated electrode surface
45 was then dried under atmospheric conditions, followed by the addition of 5 μl of
46 2-propanol solution containing 1 wt% Nafion, on the top of the catalyst layer.
47 The loadings of total metals were all controlled to 24 $\mu\text{g cm}^{-2}$.

48 The cell used was a conventional three-compartment electrochemical cell
49 containing a glassy carbon (GC) disk coated with catalyst as the working electrode,
50 platinum wire as the counter-electrode and an RHE as the reference electrode. The
51 electrolyte was a N_2 -saturated 0.5 M H_2SO_4 solution containing 0.5 M HCOOH.
52 In the CV measurements, the electrode potential was scanned in the range of
53 0.05–1.2 V versus RHE. Chronoamperometry was carried out with the working
54 electrode rotating at a speed of 200 rpm to prevent fuel starvation and bubble
55 formation on the working electrode, with its potential held at 0.3 V versus RHE, in
56 an electrolyte solution containing 0.1 M H_2SO_4 , and 0.5 M HCOOH. All the catalyst
57 electrodes were cleaned before data collection with a steady-state CV scanned for
58 three cycles in the range of 0.05–1.2 V versus RHE at 50 mV s⁻¹. All electrochemical
59 experiments were carried out at room temperature and ambient pressure.

60 Received 25 August 2009; accepted 11 January 2010;

61 published online XX XX 2010

62 References

- 63 1. Weber, M., Wang, J. T., Wasmus, S. & Savinell, R. F. Formic acid oxidation in a
64 polymer electrolyte fuel cell. *J. Electrochem. Soc.* **143**, L158–L160 (1996).
65 2. Rice, C. *et al.* Direct formic acid fuel cells. *J. Power Sources* **111**, 83–89 (2002).
66 3. Rhee, Y.-W., Ha, S. Y. & Masel, R. I. Crossover of formic acid through Nafion[®]
67 membranes. *J. Power Sources* **117**, 35–38 (2003).
68 4. Park, S., Xie, Y. & Weaver, M. J. Electrocatalytic pathways on carbon-supported
69 platinum nanoparticles: comparison of particle-size-dependent rates of
70 methanol, formic acid, and formaldehyde electrooxidation. *Langmuir* **18**,
71 5792–5798 (2002).
72 5. Lovi \acute{c} , J. D. *et al.* Kinetic study of formic acid oxidation on carbon-supported
73 platinum electrocatalyst. *J. Electroanal. Chem.* **581**, 294–302 (2005).

6. Capon, A. & Parsons, R. J. The oxidation of formic acid at noble metal
74 electrodes. Part III. Intermediates and mechanism on platinum electrodes. 75
Electroanal. Chem. **45**, 205–231 (1973). 76
7. Wolter, O., Willsau, J. & Heitbaum, J. Reaction pathways of the anodic oxidation
77 of formic acid on Pt evidenced by ¹⁸O labeling—a DEMS study. *J. Electrochem.*
78 *Soc.* **132**, 1635–1638 (1985). 79
8. Sun, S. G. & Clavilier, J. The mechanism of electrocatalytic oxidation of formic
80 acid on Pt (100) and Pt (111) in sulphuric acid solution: an emirs study. 81
J. Electroanal. Chem. **240**, 147–159 (1988). 82
9. Chang, S.-C., Ho, Y. & Weaver, M. J. Applications of real-time infrared
83 spectroscopy to electrocatalysis at bimetallic surfaces: I. Electrooxidation of
84 formic acid and methanol on bismuth-modified Pt(111) and Pt(100). *Surf. Sci.*
85 **265**, 81–94 (1992). 86
10. Llorca, M. J., Herrero, E., Feliu, J. M. & Aldaz, A. Formic acid oxidation on
87 Pt(111) electrodes modified by irreversibly adsorbed selenium. *J. Electroanal.*
88 *Chem.* **373**, 217–225 (1994). 89
11. Leiva, E., Iwasita, T., Herrero, E. & Feliu, J. M. Effect of adatoms in the
90 electrocatalysis of HCOOH oxidation. A theoretical model. *Langmuir* **13**,
91 6287–6293 (1997). 92
12. Smith, S. P. E. & Abruña, H. D. Structural effects on the oxidation of HCOOH by
93 bismuth modified Pt(111) electrodes with (110) monatomic steps. *J. Electroanal.*
94 *Chem.* **467**, 43–49 (1999). 95
13. Schmidt, T. J. & Behm, R. J. Formic acid oxidation on pure and Bi-modified
96 Pt(111): temperature effects. *Langmuir* **16**, 8159–8166 (2000). 97
14. Spendlow, J. S. & Wieckowski, A. Noble metal decoration of single crystal
98 platinum surfaces to create well-defined bimetallic electrocatalysts. *Phys. Chem.*
99 *Chem. Phys.* **6**, 5094–5118 (2004). 100
15. Casado-Rivera, E. *et al.* Electrocatalytic oxidation of formic acid at an ordered
101 intermetallic PtBi surface. *ChemPhysChem* **4**, 193–199 (2003). 102
16. Casado-Rivera, E. *et al.* Electrocatalytic activity of ordered intermetallic phases
103 for fuel cell applications. *J. Am. Chem. Soc.* **126**, 4043–4049 (2004). 104
17. Rice, C., Ha, S., Masel, R. I. & Wieckowski, A. Catalysts for direct formic acid fuel
105 cells. *J. Power Sources* **115**, 229–235 (2003). 106
18. Roychowdhury, C., Matsumoto, F., Mutolo, P. F., Abruña, H. D. & DiSalvo, F. J.
107 Synthesis, characterization, and electrocatalytic activity of PtBi nanoparticles
108 prepared by the polyol process. *Chem. Mater.* **17**, 5871–5876 (2005). 109
19. Roychowdhury, C. *et al.* Synthesis, characterization, and electrocatalytic activity
110 of PtBi and PtPb nanoparticles prepared by borohydride reduction in methanol.
111 *Chem. Mater.* **18**, 3365–3372 (2006). 112
20. Matsumoto, F., Roychowdhury, C., DiSalvo, F. J. & Abruña, H. D.
113 Electrocatalytic activity of ordered intermetallic PtPb nanoparticles prepared by
114 borohydride reduction toward formic acid oxidation. *J. Electrochem. Soc.* **155**,
115 B148–B154 (2008). 116
21. Bauer, J. C., Chen, X., Liu, Q., Phan, T.-H. & Schaak, R. E. Converting
117 nanocrystalline metals into alloys and intermetallic compounds for applications
118 in catalysis. *J. Mater. Chem.* **18**, 275–282 (2008). 119
22. Chan, K.-Y., Ding, J., Ren, J., Cheng, S. & Tsang, K. Y. Supported mixed metal
120 nanoparticles as electrocatalysts in low temperature fuel cells. *J. Mater. Chem.* **14**,
121 505–516 (2004). 122
23. Ryoo, R., Joo, S. H. & Jun, S. Synthesis of highly ordered carbon molecular sieves
123 via template-mediated structural transformation. *J. Phys. Chem. B* **103**,
124 7743–7746 (1999). 125
24. Joo, S. *et al.* Ordered nanoporous arrays of carbon supporting high dispersions
126 of platinum nanoparticles. *Nature* **412**, 169–172 (2001). 127
25. Joo, J. B., Kim, P., Kim, W., Kim, J. & Yi, J. Preparation of mesoporous carbon
128 templated by silica particles for use as a catalyst support in polymer electrolyte
129 membrane fuel cells. *Catal. Today* **111**, 171–175 (2006). 130
26. Nam, J.-H., Jang, Y.-Y., Kwon, Y.-U. & Nam, J.-D. Direct methanol fuel cell Pt–
131 carbon catalysts by using SBA-15 nanoporous templates. *Electrochem. Commun.*
132 **6**, 737–741 (2004). 133
27. Yu, J.-S., Kang, S., Yoon, S. B. & Chai, G. Fabrication of ordered uniform porous
134 carbon networks and their application to a catalyst supporter. *J. Am. Chem. Soc.* **135**
135 124, 9382–9383 (2002). 136
28. Liu, H. *et al.* A review of anode catalysis in the direct methanol fuel cell. *J. Power*
137 *Sources* **155**, 95–110 (2006). 138
29. Li, Z., Yan, W. & Dai, S. Surface functionalization of ordered mesoporous
139 carbons—a comparative study. *Langmuir* **21**, 11999–12006 (2005). 140
30. Guo, Z. *et al.* Adsorption of vitamin B12 on ordered mesoporous carbons coated
141 with PMMA. *Carbon* **43**, 2344–2351 (2005). 142
31. Calvillo, L. *et al.* Platinum supported on functionalized ordered mesoporous
143 carbon as electrocatalyst for direct methanol fuel cells. *J. Power Sources* **169**,
144 59–64 (2007). 145
32. Choi, W. *et al.* Platinum nanoclusters studded in the microporous nanowalls of
146 ordered mesoporous carbon. *Adv. Mater.* **17**, 446–451 (2005). 147
33. Wen, Z., Liu, J. & Li, J. Core/shell Pt/C nanoparticles embedded in mesoporous
148 carbon as a methanol-tolerant cathode catalyst in direct methanol fuel cells. *Adv.*
149 *Mater.* **20**, 743–747 (2008). 150

- 1 34. Liu, S. *et al.* Fabrication and characterization of well-dispersed and highly stable
2 PtRu nanoparticles on carbon mesoporous material for applications in direct
3 methanol fuel cell. *Chem. Mater.* **20**, 1622–1628 (2008).
- 4 35. Orillall, M. C. *et al.* One-pot synthesis of platinum-based nanoparticles
5 incorporated into mesoporous niobium oxide-carbon composites for fuel cell
6 electrodes. *J. Am. Chem. Soc.* **131**, 9389–9395 (2009).
- 7 36. Zhu, Y., Kockrick, E., Kaskel, S., Ikoma, T. & Hanagata, N. Nanocasting route to
8 ordered mesoporous carbon with FePt nanoparticles and its phenol adsorption
9 property. *J. Phys. Chem. C* **113**, 5998–6002 (2009).
- 10 37. Jun, S. *et al.* Synthesis of new, nanoporous carbon with hexagonally ordered
11 mesostructure. *J. Am. Chem. Soc.* **122**, 10712–10713 (2000).
- 12 38. Chen, I. Molecular-orbital studies of charge carrier transport in orthorhombic
13 sulfur. I. Molecular orbitals of S₈. *Phys. Rev. B* **2**, 1053–1060 (1970).
- 14 39. Miller, J. T. & Koningsberger, D. C. The origin of sulfur tolerance in supported
15 platinum catalysts: the relationship between structural and catalytic properties in
16 acidic and alkaline Pt/LTL. *J. Catal.* **162**, 209–219 (1996).
- 17 40. Ji, X., Lee, K. T. & Nazar, L. F. A highly ordered nanostructured carbon-sulphur
18 cathode for lithium-sulphur batteries. *Nat. Mater.* **8**, 500–506 (2009).
- 19 41. Zhuravlev, N. N. & Stepanova, A. A. An X-ray investigation of superconducting
20 alloys of bismuth with platinum in the range of 20–640 °C. *Sov. Phys.-*
21 *Crystallogr.* **7**, 231–242 (1962).
- 22 42. Blasini, D. R. *et al.* Surface composition of ordered intermetallic compounds
23 PtBi and PtPb. *Surf. Sci.* **600**, 2670–2680 (2006).
- 24 43. Zhou, W. P. *et al.* Size effects in electronic and catalytic properties of
25 unsupported palladium nanoparticles in electrooxidation of formic acid. *J. Phys.*
26 *Chem. B* **110**, 13393–13398 (2006).
- 27 44. Ge, J. *et al.* Controllable synthesis of Pd nanocatalysts for direct formic acid fuel
28 cell (DFAFC) application: from Pd hollow nanospheres to Pd nanoparticles.
29 *J. Phys. Chem. C* **111**, 17305–17310 (2007).
- 30 45. Kristian, N., Yanb, Y. & Wang, X. Highly efficient submonolayer Pt-decorated
31 Au nano-catalysts for formic acid oxidation. *Chem. Commun.* 353–355 (2008).
- 32 46. Xu, J. B., Zhao, T. S. & Liang, Z. X. Synthesis of active platinum-silver alloy
33 electrocatalyst toward the formic acid oxidation reaction. *J. Phys. Chem. C* **112**,
64 7362–7368 (2008).
47. Tian, N., Zhou, Z., Sun, S., Ding, Y. & Wang, Z. Synthesis of tetrahedral
35 platinum nanocrystals with high-index facets and high electro-oxidation activity.
36 *Science* **316**, 732–735 (2007).
- 37
48. Rigsby, M. A. *et al.* Experiment and theory of fuel cell catalysis: methanol and
38 formic acid decomposition on nanoparticle Pt/Ru. *J. Phys. Chem. C* **112**,
39 15595–15601 (2008).
- 40
49. Huang, Y. *et al.* Preparation of Pd/C catalyst for formic acid oxidation using a
41 novel colloid method. *Electrochem. Commun.* **10**, 621–624 (2008).
- 42
50. Yu, X. & Pickup, P. G. Recent advances in direct formic acid fuel cells (DFAFC).
43 *J. Power Sources* **182**, 124–132 (2008).
- 44

Acknowledgements

L.F.N. gratefully acknowledges the financial support of the National Science and
45 Engineering Research Council (NSERC, Canada) through its Discovery Grant and Canada
46 Research Chair programs. We thank R. Sodhi at Surface Interface Ontario, University of
47 Toronto, for acquisition and processing of the XPS spectra and C. Mims for helpful
48 discussions, N. Coombs at the Centre for Nanostructured Imaging, University of Toronto,
49 for help with acquisition of the STEM imaging, and C. Andrei (McMaster University,
50 Canadian Centre for Electron Microscopy) for help with the high-resolution imaging work.
51 The experimental work on the FEI Titan 80–300 and FEI Titan 80–300 Cubed was carried
52 out at the Canadian Centre for Electron Microscopy, a user facility supported by NSERC
53 and McMaster University.

Author contributions

X.J. and L.N. designed and conducted the research. Electrochemical experiments were
56 performed by X.J., L.Z., and J.Z. K.L. and R.H. contributed analysis. TEM experiments were
57 performed by G.B. and M.C. L.N. and X.J. wrote the paper.

Additional information

The authors declare no competing financial interests. Supplementary information
60 accompanies this paper at www.nature.com/naturechemistry. Reprints and permission
61 information is available online at <http://npg.nature.com/reprintsandpermissions/>.
62 Correspondence and requests for materials should be addressed to L.F.N.
63
64

Publisher: Nature

Journal: Nature Chemistry

Article number: nchem.553

Author (s): Xiulei Ji *et al.*

Title of paper: Nanocrystalline intermetallics on mesoporous carbon for direct formic acid fuel cell anodes

Query no.	Query	Response
1	Do you mean “tuned up by ~3.5 nm” or “tuned up to ~3.5 nm”. Please clarify.	
2	Changed “nano-dimensions” to “nanoscale dimensions” – OK?	
3	Please clarify what you mean by "sec" here.	
4	Fig 4c and d captions renumbered in the figure caption to correspond with the figure – please check text references carefully.	
5	Please clarify what you mean by “similarly” here.	
6		
7		
8		
9		
10		
11		
12		
13		
14		
15		
16		
17		
18		
19		